PHYSICAL SCIENCES

Body-temperature softening electronic ink for additive manufacturing of transformative bioelectronics via direct writing

Do A Kwon[1,2]†, Simok Lee[1]†, Choong Yeon Kim[1], Inho Kang[1], Steve Park[2,3]*, Jae-Woong Jeong[1,3]*

Mechanically transformative electronic systems (TESs) built using gallium have emerged as an innovative class of electronics due to their ability to switch between rigid and flexible states, thus expanding the versatility of electronics. However, the challenges posed by gallium's high surface tension and low viscosity have substantially hindered manufacturability, limiting high-resolution patterning of TESs. To address this challenge, we introduce a stiffness-tunable gallium-copper composite ink capable of direct ink write printing of intricate TES circuits, offering high-resolution (~50 micrometers) patterning, high conductivity, and bidirectional soft-rigid convertibility. These features enable transformative bioelectronics with design complexity akin to traditional printed circuit boards. These TESs maintain rigidity at room temperature for easy handling but soften and conform to curvilinear tissue surfaces at body temperature, adapting to dynamic tissue deformations. The proposed ink with direct ink write printing makes TES manufacturing simple and versatile, opening possibilities in wearables, implantables, consumer electronics, and robotics.

INTRODUCTION

Electronics today have evolved substantially, fulfilling the diverse needs of our society using various materials, either rigid or soft. Rigid materials are mainly used in portable and user-friendly handheld interfaces such as smartphones and tablets (*1*, *2*). In contrast, soft materials hold immense promise for wearable applications owing to their inherent flexibility and their ability to seamlessly conform to the contours of the human body (*3*–*7*). However, a challenge persists: The fixed mechanical stiffness of modern electronics restricts their broad utility. Rigid electronics struggle to adapt to our skin or organs, while soft electronics lack the stiffness necessary to bear loads effectively. Recently, a potential solution to this issue has emerged in the form of a "transformative electronic system (TES)" (*1*, *2*, *8*–*12*) capable of converting between rigid and soft electronics. TES has demonstrated boundless potential in enhancing the adaptability, convenience, and versatility of electronics for various applications through facile tuning of stiffness and stretchability.

TES designs typically use complex multilayer structures comprising flexible, stretchable electronic layers integrated onto a stiffness-tuning platform constructed from stimuli-responsive materials (*1*, *2*, *9*, *12*). However, this approach demands complex fabrication and integration of the multiple, functionally distinct layers, resulting in inefficient processing and production of bulky devices. TES circuit boards that can effectively function as both an electronic layer and a mechanically tunable platform have the potential to overcome this challenge. Therefore, there is a pressing need to explore a wide range of stimuli-responsive materials and their manufacturing techniques that can bring this innovation to realization.

Stimuli-responsive materials for these dual-function TES circuit boards must satisfy three key criteria: (i) high stiffness tunability, (ii) high conductivity, and (iii) high-resolution patternability. These factors are pivotal and are typically influenced by the properties of stimuli-responsive materials incorporated into the system. While various stimuli-responsive materials have been explored, including electroactive polymers (*13*), magnetoactive matter (*14*), and thermally induced materials (*15*), liquid metal gallium (Ga) stands out, particularly in TES applications related to biological contexts. This is due to its impressive properties, including excellent mechanical tuning ability (~0 Pa in liquid state and 9.8 GPa in solid state) (*1*, *9*), exceptional electrical conductivities (3.4×10^6 S m^{-1}) (*16*), low toxicity (*1*, *17*), and a phase change at physiological temperature. Ga undergoes a phase transition at 29.76°C, making it suitable for TES for wearable and implantable applications, as its melting temperature falls between room temperature (25°C) and body temperature (36.7°C). Despite its numerous merits as a promising material for TES, Ga encounters challenges in high-resolution patterning due to its high surface tension and low viscosity (*18*). This obstacle restricts the available patterning methods to mold casting (*1*–*3*, *19*) or polymer encapsulation (*8*, *9*), hindering the high-resolution construction of TES circuit boards compatible with standard printed circuit boards. As a result, Ga has primarily served as a foundational transformative framework in applications such as neural probes (*1*), wearables (*1*, *9*, *12*), and pressure sensors (*8*). However, the construction of densely integrated TES with high-resolution electronic circuits remains an unsolved terrain for Ga.

Several high-resolution liquid metal patterning techniques have been proposed for use in device applications, yet none have proven effective in fabricating printed circuit board–level TES using Ga ink-based methods, such as screen printing with prepatterned stencils (*20*) and inkjet printing with piezoelectric or thermal transducers to eject ink droplets (*21*, *22*), offer potential solutions. Nevertheless, screen printing complicates processing as it requires rigid masks (*22*, *23*), and inkjet printing often leads to unstable, defective patterns due to ejection issues (*22*). Moreover, both methods are limited to

[1]School of Electrical Engineering, Korea Advanced Institute of Science and Technology (KAIST), Daejeon 34141, Republic of Korea. [2]Department of Materials Science and Engineering, Korea Advanced Institute of Science and Technology (KAIST), Daejeon 34141, Republic of Korea. [3]KAIST Institute for Health Science and Technology, Daejeon 34141, Republic of Korea.
*Corresponding author. Email: jjeong1@kaist.ac.kr (J.-W.J.); stevepark@kaist.ac.kr (S.P.)
†These authors contributed equally to this work.

two-dimensional (2D) flat structures and cannot be extended to 3D freeform designs (*24*). In contrast, direct ink write (DIW) printing is a promising technique that uses microscale nozzles and prepatterned digital masks to extrude viscoelastic ink onto substrates, allowing precise patterning of preprogrammed designs with high resolution (*25*). Its additive patterning mechanism enables the construction of 3D freeform structures of various sizes on diverse substrates. Despite these advantages, DIW is not suitable for Ga due to undesirable ink behaviors such as printed lines merging and ink spreading during extrusion. Previous efforts to address these issues involved adding nonmetallic fillers (*26*) or creating Ga microgranule–elastomer composites (*8*). While both methods increased viscosity, overly viscous ink clogs the nozzles, making it unsuitable for DIW. Moreover, incorporating nonconductive materials resulted in poor conductivity.

Here, we present a one-step preparable, stiffness-tunable gallium-copper (Ga-Cu) composite electronic ink designed for nozzle-based DIW printing of high-resolution TES circuit boards, functioning both as electronic layers and mechanically transformative frameworks. Prior research attempted incorporating a high copper content [18–52 weight percentage (wt %) of Cu] in Ga to achieve rapid hardening of the composite ink (within 60 min at 60°C) into solid intermetallic phases ($CuGa_2$) for high-resolution printing (*27*). However, this ink lacks the essential stiffness tunability crucial for TES fabrication and is prone to nozzle clogging during nozzle-based direct write printing. To overcome this issue, we developed a Ga-Cu composite ink with an optimized low wt % of Cu, which does not solidify through intermetallic formation even after months of storage while facilitating microscale printing with excellent uniformity. We also ensured high-resolution printing by fine-tuning the ink's properties, including wettability, viscosity, and surface tension, through a systematic study of Cu wt % in the Ga base. The printed Ga-Cu composite ink yields patterns with exceptional characteristics: (i) high stiffness tunability (stiffness tuning ratio, 990 for 150-μm-thick device), (ii) high electrical conductivity (3.69×10^6 S m^{-1} at 5.0 wt % of Cu; ~8% increase than bulk Ga), and (iii) high-resolution (~50 μm) patternability. The fabricated TES device demonstrates a temperature-dependent phase transition, enabling bidirectional stiffness tuning, crucial for TES functionality. We showcased these features through the operation of two devices: (i) an ultrathin epidermal photoplethysmography (PPG) device for blood pulse sensing and (ii) an intricately designed wireless optoelectronic device. These transformative devices maintain stiffness at room temperature for easy handling yet seamlessly conform to the skin's wrinkles and curvatures at body temperature. They also highlight high-resolution patterning and precise control over widths and thicknesses. The combined merits of this one-step preparable, stiffness-tunable ink and the rapid, high-resolution direct write printing method simplify TES construction, opening new opportunities in this field.

RESULTS

Overview on direct-write printing of stiffness-tunable Ga-Cu composite ink for versatile additive manufacturing of TES

Figure 1 and table S1 highlight the key advantages offered by direct-write printing of one-step preparable Ga-Cu composite ink for TES. The Ga-Cu composite ink is prepared by a single-step, solvent-free sonication of liquid Ga and Cu fillers (spheroidal diameter, 10 to 25 μm) with an optimal weight percentage (5.0 wt %). The Cu fillers serve as rheological modifiers by enhancing ink viscosity and reducing the surface tension of Ga for its high-resolution patterning. These fillers also improve heat transfer owing to its high thermal conductivity (320.72 W m^{-1} K^{-1}) (*28*) and serve as nucleating agents, facilitating rapid phase transitions between solid and liquid states. The ink stands out for its simplicity in preparation. Unlike conventional methods that require laborious preprocessing [e.g., acid treatment (*29*) and vacuum drying (*30*)] or postprocessing steps [e.g., calcination (*29*)], our Ga-Cu composite ink does not require harsh treatments. High printability, tunable stiffness, and ease of processing of Ga-Cu composite make it an ideal building block for high-resolution printing of a functional TES.

Direct-write printing using this ink offers versatile production capabilities for TES in several ways. First, it leverages additive manufacturing, enabling excellent printability on a wide range of substrates, including very high bonding (VHB) clear tape (3M), paper, tape, foam tape (3M), poly[styrene-*b*-(ethylene-*co*-butylene)-*b*-styrene] (SEBS), polydimethylsiloxane (PDMS), polyimide (PI) film, and scotch tape, as depicted in Fig. 1A (a). The versatility, coupled with the absence of harsh postprocessing, makes direct-write printing ideal for universal applications. Moreover, the preprogrammed printer nozzle movement allows for patterning customized devices with various sizes (Fig. 1A, b), and the ink's shape-retaining characteristic at room temperature enables printing of highly conductive, free-standing, bridge-type structures without requiring mechanical support (Fig. 1A, c, and fig. S1A) (*31*). The exceptional conductivity of the ink enables the direct integration of mechanically tunable electrical circuits with electronic components, eliminating the need for additional circuit layers (*1*, *9*). Last, line widths/thicknesses can be easily controlled with ultrahigh precision by manipulating process parameters, such as printing speed, extrusion rate, and nozzle size (*23*), allowing for a minimum pattern resolution of 50 μm (Fig. 1A, d, and fig. S1B).

Direct-write printing of Ga-Cu composite ink creates a synergistic effect that enhances the fabrication of functional, high-resolution TES with faster and bidirectional phase transition. The mode conversion, based on the solid-liquid phase transition of Ga-Cu composite ink (melting temperature of 27°C), offers distinct merits for our TES in each mode (*32*). At room temperature or below (<25°C), Ga-Cu composite stays in its solid state, making the device stiff and easy to handle, referred to as "rigid mode" (Fig. 1B, left). When exposed to body temperature (36.7°C), Ga-Cu composite transforms into a liquid state, allowing the device to become flexible and perfectly conform to body contours. This transformation, referred to as the "soft mode" (Fig. 1B, right), enables robust, high-fidelity sensing of physiological signals through intimate device-body integration. Notably, the device transitions rapidly from rigid to soft mode when exposed to body heat (~40 s at 36.7°C) and can revert to its initial rigid state when exposed to a cold atmosphere (~180 s at 1°C). The body heat–triggered, bidirectional, and fast mechanical tuning, coupled with high resolution, high conductivity, and design versatility, expands the potential of the TES beyond previously demonstrated capabilities (*1*, *2*, *8*, *9*, *12*).

Systematic study of stiffness-tunable Ga-Cu composite ink

Our stiffness-tunable Ga-Cu composite ink is created by dispersing 5.0 wt % of Cu fillers (10 to 25 μm) into liquid Ga using a tip sonicator (Fig. 2A, left, and fig. S2). We evaluated various metal filler candidates, including silver (Ag), nickel (Ni), and copper (Cu), and Cu emerged as the most suitable choice for our electronic ink composite due to its high electrical conductivity (fig. S3), excellent thermal

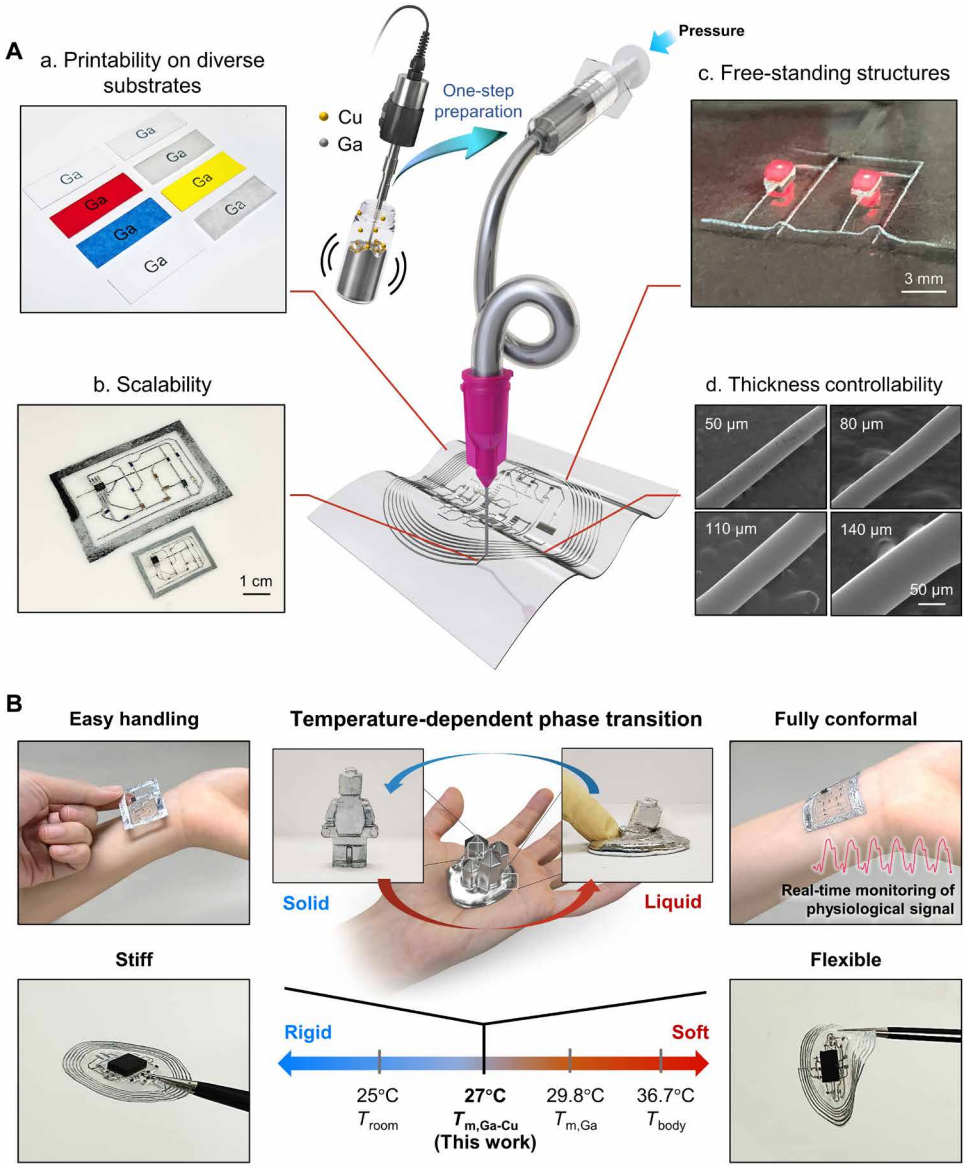

Fig. 1. Overview of direct-write printing of one-step preparable and stiffness tunable Ga-Cu composite ink for versatile additive manufacturing of mechanically transformative electronics. (**A**) Schematic illustration of direct-write printing of Ga-Cu composite ink and its key characteristics. (a) Printability on different substrates. Substrates from top left to bottom right: glass, VHB tape, paper tape, foam tape, SEBS, PDMS, PI film, and scotch tape. (b) Scalability of printed electronics (length × width: small version, 3.2 cm × 2.2 cm; large version, 8.0 cm × 5.2 cm). (c) Omnidirectional printing capability. A free-standing 3D circuit demonstrated using a 1 × 2 light-emitting diode (LED) array (step height of the arched interconnects, 400 μm). (d) Thickness controllability. Different thicknesses of ink (50, 80, 110, and 140 μm) controlled by the printing speeds. (**B**) Conceptual illustration and images of transformative electronics based on Ga-Cu composite ink demonstrating its mechanical characteristics in two convertible modes—rigid and soft modes. Through the mode conversion based on the solid-liquid phase transition of Ga-Cu composite ink, the electronics is stiff and can easily be handled in the rigid mode, while being flexible and highly conformable in the soft mode, respectively.

conductivity (320.72 W m^{-1} K^{-1}) (*28*), and low cost. During sonication, the shear forces and the cavitation effect of acoustic energy generated by the probe tip break the oxide skin of Ga and disperse the Cu fillers within it (fig. S4) (*33*). In addition, heat generated from the vibrating tip keeps Ga in the liquid state, further facilitating its thorough mixing with Cu fillers (Fig. 2A, right). As a result, sonication time significantly affects the uniformity of Cu filler dispersion. Figure 2B compares the energy-dispersive x-ray spectroscopy (EDS)–mapped images of Ga-Cu composites after tip sonication for 1 and 5 min. While a 1-min sonication causes poor-resolution printing or nozzle clogging due to nonuniform dispersion and local aggregation of Cu fillers (Fig. 2B, bottom left), a sufficiently long sonication time (5 min or more; fig. S5) achieves the uniform dispersion of Cu fillers (Fig. 2B, bottom right).

Ga ink mixed with homogeneously dispersed Cu fillers shows an increased viscosity and a reduced surface tension within a printable range (Fig. 2C), facilitating uniform printing of lines, and ensures an effective phase transition of Ga-Cu composite ink. Unlike pure Ga

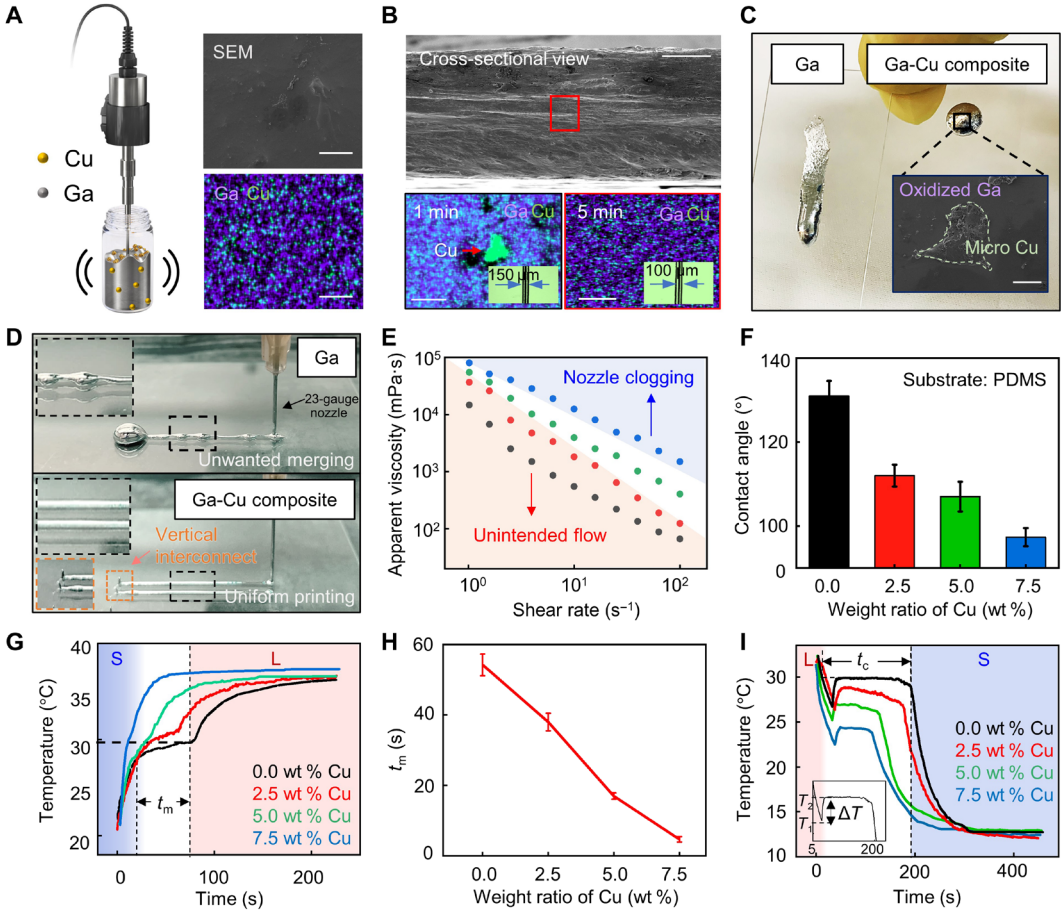

Fig. 2. Chemical, rheological, and thermal characterization of mode-convertible Ga-Cu composite ink. (**A**) Schematic of the ink fabrication process via one-step sonication (left), scanning electron microscope (SEM; top right) image and EDS (bottom right) mapping of Ga-Cu composite ink showing uniformly dispersed Cu fillers in Ga. (**B**) Top: SEM image showing cross section of a line printed with ink sonicated for 5 min. Bottom: EDS images of lines printed with inks subjected to different sonication times. One-minute sonication (bottom left) forms Cu filler agglomerates (pointed with a red arrow), causing clogging or thicker lines compared to 5-min sonication (bottom right). (**C**) Comparison of a 1-ml droplet of pure Ga and Ga-Cu composite ink on a tilted glass substrate. Inset: SEM image depicting ink composition. (**D**) Printed lines using pure Ga (top) and Ga-Cu composite ink (bottom). The composite ink prints uniformly and creates out-of-plane vertical interconnects without merging or clogging. The inset shows a magnified image of the printed line. (**E**) Apparent viscosity of ink with different weight percentages of Cu: 0.0 wt % (black), 2.5 wt % (red), 5.0 wt % (green), 7.5 wt % (blue). (**F**) Contact angles of Ga-Cu composite ink with various weight percentages of Cu (0.0, 2.5, 5.0, 7.5 wt % of Cu). Contact angle decreases with higher weight percentage of Cu, enhancing ink wettability on substrates ($N = 4$ samples). (**G**) Plot illustrating the solid-to-liquid phase transition of the ink with different weight percentages of Cu. (**H**) Solid-to-liquid phase transition time (t_m) for the ink with different weight percentages of Cu. Cu fillers reduce t_m. (**I**) Plot illustrating the liquid-to-solid phase transition of the ink with different weight percentages of Cu. Samples were initially thawed at 45°C for 20 min upon reaching equilibrium temperature (*61*) and were cooled at 5°C. Cu fillers shortens both the transition time (t_c) and the degree of supercooling (ΔT). Scale bars, 20 μm.

that is challenged by undesirable merging and nonuniformity during printing (Fig. 2D, top), the Ga-Cu composite ink not only produces uniform lines but also creates pillar-shaped vertical interconnects by synchronizing the withdrawal speed of the nozzle tip and the growth rate of the printed lines (Fig. 2D, bottom). To further optimize the printing performance, we investigated the viscosity of Ga-Cu composites with different wt % of Cu fillers. According to Fig. 2E, addition of Cu in Ga increases the viscosity of Ga-Cu composite. A low viscosity, similar to that of water, can result in unintended ink flow from the nozzle due to the gravitational force upon nozzle lifting, while highly viscous ink can clog the nozzle tip due to its shear-thickening characteristic. To this end, we determined to maintain 5.0 wt % of Cu fillers to mitigate these rheological issues (i.e., unintended ink flow and nozzle clogging) and to optimize the printing performance.

To achieve high-resolution printing, Ga-Cu composite ink demands rheological attributes beyond high viscosity, specifically low surface tension and high wettability on substrates. As depicted in Fig. 2F, addition of Cu fillers to Ga reduces the contact angle (θ) of an ink droplet on a PDMS substrate. This decrease in contact angle indicates a lower surface tension and an improved wettability to substrates. Enhanced wettability with incorporated Cu fillers ensures reliable printing of high-quality electrical traces, preventing common printing issues such as disconnected droplets or coalesced printed lines in pure Ga. Further investigation involves contact angle measurements of Ga-Cu composite droplets on different substrates (e.g., PDMS, glass, and PI film), showing a consistent decrease in contact angle upon incorporation of Cu (fig. S6).

Investigation into thermal behaviors reveals that Cu fillers effectively facilitate the solid-liquid phase transition of Ga-Cu composite

ink, leading to an efficient mode conversion of TES. Cu has a high thermal conductivity (320.72 W m^{-1} K^{-1}), which significantly outperforms Ga (29.31 to 37.68 W m^{-1} K^{-1}) (*34*, *35*). Consequently, incorporating Cu substantially enhances the thermal conductivity of the ink, giving rise to a thermal behavior resembling that of a pure metal (Fig. 2G). While pure Ga shows a clear solid-to-liquid phase transition at ~29.8°C, Ga-Cu composite demonstrates a faster transition with a higher concentration of Cu fillers. The accelerated phase transition is evident from the reduced phase transition time (t_m; from solid to liquid), as shown in Fig. 2H. Specifically, incorporating 5.0 wt % of Cu decreases the phase transition time by 31% (from 54.19 to 16.96 s) compared to pure Ga. Figure 2I illustrates the freezing behavior of Ga-Cu composites at 5°C, where t_c denotes the characteristic phase transition time for liquid-to-solid conversion. Figure S7A illustrates that increasing Cu wt % reduces both phase transition temperature, T_2, and degree of supercooling, ΔT. In addition, t_c (fig. S7B) decreases with the introduction of Cu fillers as Cu enhances thermal conductivity, which aligns with the observed decrease in t_m during the melting process. These thermal characteristics highlight the advantages of Ga-Cu composite ink for phase conversion and demonstrate that incorporation of Cu fillers facilitates a faster and reversible rigid-soft mode conversion of TES by effectively enhancing thermal conductivity and mitigating the degree of supercooling.

Systematic study on printing conditions and electromechanical characterization of printed TES

A systematic study of printing conditions tailored to the rheological properties of ink not only enhances printer resolution but also introduces diversity to printable designs. Our customized 3D printer, shown in fig. S8, prints Ga-Cu composite ink through four main steps: (i) initial contact, (ii) direct printing, (iii) fast lift-off, and (iv) release (Fig. 3A). A detailed view of the direct printing and lift-off phases is schematically illustrated in Fig. 3B. The direct-write printing operates through additive manufacturing, which deposits materials layer by layer, facilitating successful printing of Ga-Cu composite ink on various substrates, including VHB tape, SEBS, glass, and PDMS (Fig. 3C).

The widths, thicknesses, and vertical height of the printed pattern can be adjusted by manipulating printing parameters, allowing precise control over the printing output. The vertical height of the printed structure depends on the speed at which the nozzle lifts off (*24*). A slow lift-off (10 mm s^{-1}) forms tall vertical interconnects (~3 cm; fig. S9), and a fast lift-off (25 mm s^{-1}) generates short vertical pillars (~2 mm; Fig. 3A, 3). When vertical interconnects are not necessary, further increasing the lift-off rate (>30 mm s^{-1}) leads to immediate fracture of the line as the nozzle detaches from the substrate. In this 3D printer configuration, the pattern thickness can also be precisely adjusted by changing various parameters such as printing speed (Fig. 3D), tube diameter (fig. S10A), extrusion rate (fig. S10A), extrusion pressure (Fig. 3E), and nozzle size (e.g., 23, 25, 27, and 32 gauge). To avoid unfavorable printing issues (e.g., disconnected droplets or bead-on-string patterns on a substrate) caused by Rayleigh instability (*36*), we identified the optimal range of printing conditions, including printing speed and extrusion pressure (Fig. 3F and fig. S10B).

To ensure the feasibility of printed TES in both soft and rigid modes, a comprehensive understanding of their mechanical characteristics is crucial, including bending stiffness, stretchability, and durability. Bending stiffness was measured for TES platforms of three different thicknesses (50, 100, and 150 μm), encapsulated with 50-μm-thick PDMS layers on top and bottom (Fig. 3G), and was then compared with the simulated values (fig. S11). Despite the microscale thickness, a substantial increase in stiffness tuning ratio is observed with thicker devices. For example, 150-μm-thick samples showed stiffness tuning ratio of 990, indicating a high bending stiffness of 1.53×10^{-3} N·m^2 in rigid mode and low bending stiffness of 1.55×10^{-6} N·m^2 in soft mode.

Figure 3H illustrates the stiffness tunability of TES using Ga-Cu composite interconnects, encapsulated with highly stretchable VHB tape and powered through current supplied for light-emitting diode (LED) operation. In the rigid mode at room temperature (~ 25°C), the device can withstand a 400-g weight, whereas in soft mode, it can be stretched up to 44% strain under the same load. TES integrated with LEDs in both rigid and soft modes shows high conductivity of Ga-Cu composite as demonstrated through a four-point probe method (fig. S12). A slightly lower electrical conductivity is observed for the composite at liquid phase due to a larger thermal motion of atoms and scattering of electrons, making charge transport less efficient (*37*). In addition, a stretchability test (Fig. 3I) demonstrates that the device stretches up to 652% strain in the soft mode, showcasing remarkable stretchability that is 81.5 times greater than in rigid mode. Figure 3J reveals the softened device enduring 5000 cycles of 100% strain while maintaining resistance with negligible changes. In summary, Ga-Cu composite ink-printed TES demonstrates high bending stiffness (two to three orders of magnitude greater than in soft modes) and rigidity in rigid modes, along with impressive stretchability and long-term stability under dynamic stretching in soft modes. Even after rigid electrodes crack under 100% strain, they seamlessly reconnect upon heating (fig. S13). Ga-Cu composite maintains its conductivity in both soft and rigid modes, making it highly suitable for versatile electronic applications.

Demonstration of transformative ultrathin epidermal PPG sensor

Our Ga-Cu composite ink has several distinguishing features such as facile stiffness tunability, versatile printability, and high conductivity, making it highly suitable for fabricating bioelectronic devices adaptable with tissue deformation upon integration. To illustrate its potential, we have developed a transformative epidermal PPG sensor using our electronic ink (Fig. 4A). Epidermal electronic system (EES) is a class of ultrathin, skin-conformable, and stretchable electronics capable of acutely sensing physiological signals under dynamic skin deformation (*3*, *38*–*40*). While EES maximizes user comfort by allowing imperceptible wear, its ultrathin and skin-like characteristics often cause the device to crumple before application on the skin. This necessitates temporary rigid carrier substrates to be used for proper transferring to target position (*3*, *38*, *39*, *41*), which introduces cumbersome steps into the fabrication and implementation of EES.

To address this issue, we propose a standalone ultrathin device (with a thickness of 20 μm) that not only can be easily handled without additional stiffening platforms [i.e., polyvinyl alcohol layers (*3*, *38*, *40*, *42*), silk layers (*43*), etc.] but also adapts seamlessly to wrinkles and deformations on the skin (fig. S14) through a swift rigid-to-soft mode conversion, simplifying its overall fabrication and usage. The high conductivity and microscale-level printability of our Ga-Cu composite ink further enable high-resolution printing of a multilayered electrical circuit for a transformative PPG device, which includes

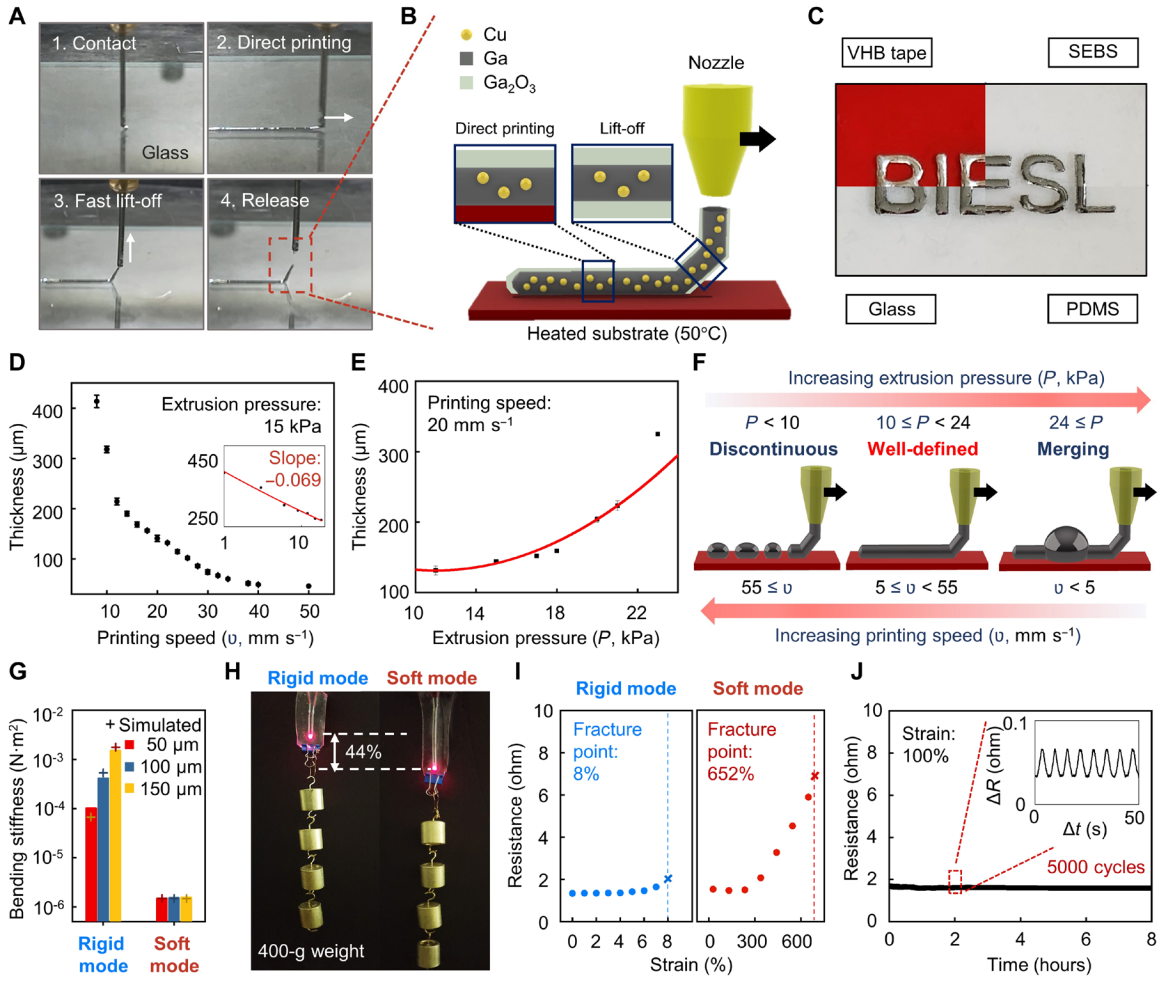

Fig. 3. A systematic study on printing conditions and electromechanical characteristics of printed Ga-Cu composite ink. (**A**) Four-step direct-write printing. The nozzle contacts the substrate (step 1) and moves autonomously along preprogrammed coordinates for printing (step 2). Then, slowly lifted off (step 3) and released (step 4). (**B**) Schematics showing direct-write printing of Ga-Cu composite ink. (**C**) The letters "BIESL" printed on different substrates, highlighting the ink's versatility. From top left to right: VHB tape and SEBS. From bottom left to right: glass and PDMS. (**D**) Thicknesses of Ga-Cu composite ink printed at different printing speeds, achieving a minimum of 50 μm. Extrusion pressure was maintained at 15 kPa using a 25-gauge needle. (**E**) Plot illustrating the line thickness relative to extrusion pressure at printing speed of 20 mm s^{-1}. Minimum line thickness of 131 μm was achieved at extrusion pressure of 10 kPa with a 25-gauge needle. (**F**) Schematics illustrating poorly printed lines when extrusion pressure and printing speed fall outside the optimized range, while well-defined lines are uniformly printed at extrusion pressures between 10 and 24 kPa and printing speeds between 5 and 55 mm s^{-1}. (**G**) Bending stiffness of printed devices with different thicknesses ($t_{Ga\text{-}Cu}$; 50, 100, and 150 μm) encapsulated in 50-μm-thick PDMS. Bar graphs and the cross marks each represent experimental data and simulation results obtained in fig. S11. (**H**) Comparison of mechanical characteristics of a transformative LED device in its rigid and soft modes, powered through printed Ga-Cu composite interconnects. LED device stretches by 44% in soft mode, while maintaining its shape in rigid mode under a uniaxial load of 400 g. (**I**) Resistance of the printed Ga-Cu transformative interconnects under strain. (**J**) Resistance of the printed transformative interconnect at soft mode, under repeated application of 100% strain over 5000 cycles.

13 surface mount device (SMD) components and 2 vertical interconnect accesses (VIAs) (Fig. 4B). Detailed circuit design and the fabrication process of our device can be found in the Materials and Methods section and figs. S15 and S16.

Our transformative epidermal PPG device demonstrates bidirectional phase transition triggered by body temperature. The Ga-Cu composite used in TES remains rigid at room temperature (~25°C) but smoothly transitions to a flexible state at body temperature (~36.7°C) within only about 40 s (Fig. 4C and movie S1). Initially, rigid epidermal device is precisely placed in desired positions on the body without structural collapse. Once attached to the skin, the PPG device softens and provides mechanical properties that match with the skin, allowing it to dynamically accommodate the skin's stretching and compression (Fig. 4D). As opposed to bulky or hardly portable rigid devices, tattoo-like ultrathin epidermal electronics shows an intimate integration to the skin, which guarantees long-term wearability and comfort in real-life settings. Furthermore, the printed interconnects have a consistent and high conductivity enough to operate the functional circuit, including capacitors, resistors, an inverting amplifier, an LED, and a photodiode, for high-fidelity sensing of blood pulse rate (Fig. 4, E and F). After pulse sensing, our PPG device can be reused through a simple process: freezing the device in a cold atmosphere (~1°C) for 3 min, as demonstrated in Fig. 4G and movie S2. Alternatively, after the measurement is

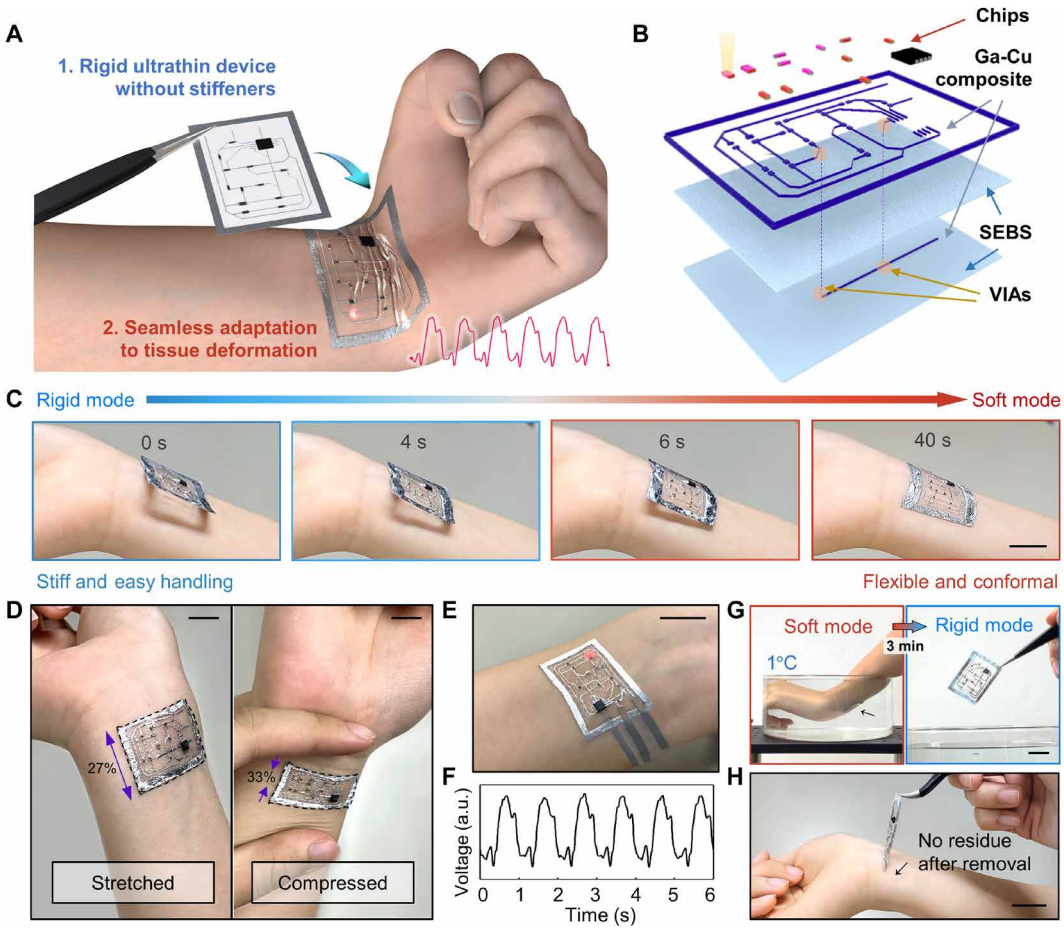

Fig. 4. Transformative epidermal PPG sensor created using mode-convertible Ga-Cu composite ink. (**A**) A schematic illustration showing how the transformative PPG sensor can be handled and worn through rigid-soft mode conversion. Initially, the ultrathin epidermal sensor is rigid and flat and can be easily handled and positioned at target position on the skin without the need for any additional stiffeners. Over time, it seamlessly conforms to the curvatures of the skin as it softens because of the body heat, which occurs through the phase transition of the Ga-Cu composite. (**B**) An exploded-view schematic diagram of a transformative epidermal PPG sensor. (**C**) Sequential images of a body temperature–triggered transformative epidermal PPG sensor (3.2 cm by 2.2 cm) as it softens and conformally adheres to the skin in 40 s. A rigid-mode PPG sensor placed on the skin gradually converts to the soft mode due to the body heat and becomes fully conformal. Scale bar, 1.5 cm. (**D**) Optical images of stretching (left) and compression (right) of the transformative device after being softened on the skin. The ultrathin device substrate (20 μm) allows it to remain fully conformal under dynamic deformation, without delamination or electrical short. Scale bars, 1 cm. (**E**) Optical image of the PPG sensor measuring the blood pulse rate from the radial artery on the wrist. Scale bar, 1.5 cm. (**F**) PPG signal measured from the radial artery. a.u., arbitrary units. (**G**) After use, the softened PPG sensor can be reused by cooling it in cold water (temperature, ~1°C) for 3 min, after which the device becomes stiff and rigid. Scale bar, 1.5 cm. (**H**) Photograph of the soft PPG sensor being peeled off from the skin for disposal. Scale bar, 1.5 cm.

completed, the softened PPG device can be easily peeled off from the skin for disposal (Fig. 4H).

Demonstration of compact transformative wireless optoelectronic device with complex trace designs

Our Ga-Cu composite ink can also be used to fabricate highly sophisticated transformative electronic circuit devices through precise control over the widths and thicknesses of electronic traces during DIW printing. To demonstrate the proof of concept, we designed a transformative wireless optoelectronic device featuring varied widths and thicknesses of electronic traces in high resolution that connect different circuit components. Our wireless optoelectronic device comprises three main parts: (i) a circular coil antenna (inner diameter, 27 mm; outer diameter, 36 mm; six turns on a single layer) to receive power wirelessly, (ii) a DC voltage quadrupler circuit containing five pairs of a Schottky diode and a capacitor to amplify the received radio frequency (RF) signal fourfold and then convert into DC power to stably charge an integrated lithium polymer (LiPo) battery (GMB-300910, PowerStream Technology; 12 mA·hour), and (iii) a wireless communication circuit integrated with a Bluetooth low-energy system on chip (BLE SoC; RFD77101, RF Digital Corporation) to allow a wireless control of a device (Fig. 5A). As shown in Fig. 5B, this device is constructed in the form of a bilayer circuit printed with Ga-Cu composite ink, with each layer being interconnected by 15 VIAs, and it includes 17 SMD components (seven capacitors, two resistors, five Schottky diodes, an LED, a voltage regulator, and a BLE SoC) and a LiPo battery. Because of this design, our wireless optoelectronic device is capable of wireless battery charging through inductive coupling, and, using the power generated from this, it can operate the integrated LED through BLE control,

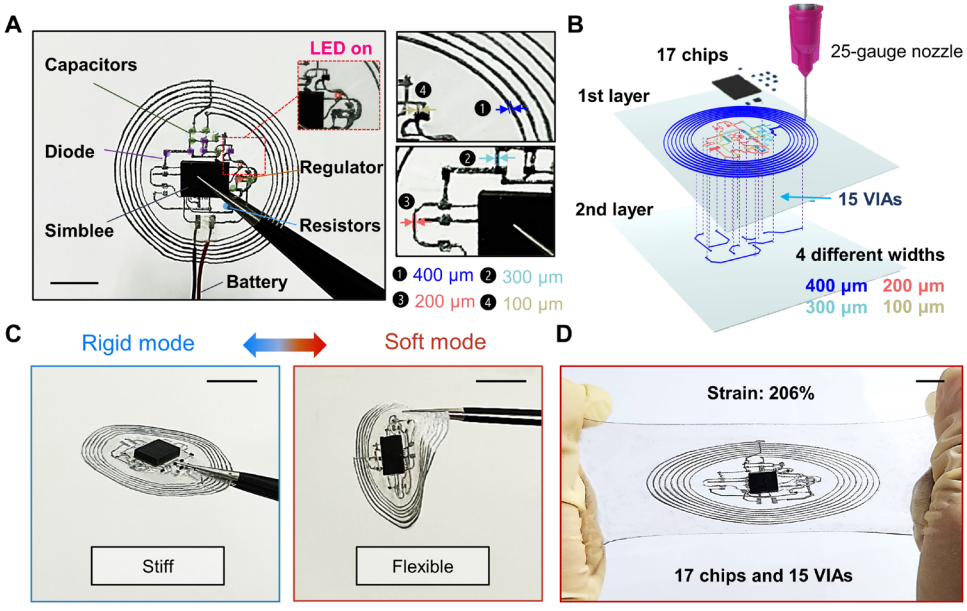

Fig. 5. Transformative wireless optoelectronic device featuring sophisticated circuit design with varied trace widths and high circuit density. (**A**) Optical image (left) of a transformative high density–integrated optoelectronic device with various trace widths, created through serial printing of the Ga-Cu composite ink for proof of demonstration. The top right image shows the antenna coils (❶) and interconnect lines (❹) printed with widths of 400 and 100 μm, respectively. The bottom right image shows interconnect lines with widths of 300 μm (❷) and 200 μm (❸). Line widths and thicknesses can be dynamically controlled during printing. Scale bar, 1.5 cm. (**B**) Schematic illustration of a bilayered transformative optoelectronic device with high chip density. This circuit includes 15 VIAs and 17 electronic components within a compact footprint (circular, 36 mm by 36 mm by 0.1 mm). (**C**) Images of the printed device demonstrating its bidirectional mechanical tunability between rigid (left) and soft (right) modes. Scale bars, 2.5 cm. (**D**) Uniaxial stretching of transformative high-density optoelectronic device (with chips) in soft mode, showing that the printed circuit remains intact on the substrate, withstanding 206% strain. Scale bar, 1 cm.

allowing for optical stimulation for potential applications in optogenetics and phototherapy. Further details of the circuit design are illustrated in the Materials and Methods section.

Here, the trace thickness of our optoelectronic device was determined by taking into account the skin effect (*44*, *45*), a crucial phenomenon in RF circuit design to prevent wasting of wirelessly transferred power. When RF current flows through a conductor wire, the current density near the surface of the wire increases with frequency, and the majority of the current flows within a "skin depth" from the surface. Derived from RF power frequency used for wireless power transfer (13.56 MHz, following the Near-Field Communication standard) and the resistivity of our Ga-Cu composite (2.71×10^{-7} ohm·m at rigid mode and 4.90×10^{-7} ohm·m at soft mode), the skin depths were calculated as 71.15 and 95.67 μm at rigid and soft modes, respectively. Since skin effect reduces the effective cross-sectional area of the conductor, increasing heating and power loss in the coil antenna (*46*), the trace thickness has to be thinner than twice the skin depth (i.e., the sum of the trace thicknesses through which current flows on the top and bottom of the conductor), which is ~142 μm at rigid mode, to minimize such an effect and ensure efficient wireless power transfer in both soft and rigid modes (*47*). Accordingly, we maintained a uniform thickness of 100 μm by keeping a consistent distance between the nozzle tip and the substrate throughout printing.

Meanwhile, the interconnects were patterned in a single printing step with varying trace widths (100 to 400 μm) at a high resolution (figs. S17 and S18). This level of precision is achieved through the optimized rheological properties of the Ga-Cu composite, as discussed in the earlier section (Fig. 2). Here, a wide range of trace widths enables both compact, miniaturized electronic circuit design and reliable, wireless power delivery. Elaborate lines with narrow widths (e.g., 100 or 200 μm) are used throughout the circuit to enhance chip density, and larger widths (e.g., 300 or 400 μm) are applied to power lines (e.g., antenna coil, power supply lines, and common ground lines) to decrease power loss of the circuit and enhance stability of the electronic device by reducing the wire resistance and enhancing the heat dissipation from the trace (*48*).

Furthermore, the Ga-Cu composite exhibits bidirectional transitions between rigid and soft modes, providing the required rigidity for shape holding until it reaches the target position, while also providing the flexibility required for adaptation to exposed curvilinear surfaces (Fig. 5C). By using soft and stretchable VHB tape (3M; shear modulus, 0.6 MPa) (*49*) as the substrate, the device in soft mode exhibits remarkable stability, withstanding a uniaxial strain of 206% (Fig. 5D). Biaxial stretching of the device emphasizes the robust adhesion of printed electronic circuits to the substrate while preserving its high-resolution patterns (fig. S19). This versatile property is highly advantageous for both implantable and wearable applications, as it allows for tunable stiffness, facilitating easy handling and seamless integration with soft tissue. For instance, the conceptual wireless transformative optoelectronics demonstrated here can be used as implantable devices for optogenetics (*50*–*55*) and phototherapy (*56*–*58*), with minimal stress on surrounding tissue.

The exceptional rheological property, mechanical tunability, and high electrical conductivity of Ga-Cu composite, coupled with the microscale precision of the high-resolution DIW method, present a promising pathway for advancing mechanically transformative electronics. This transformative technology holds the potential to

revolutionize bioelectronics, focusing on human-centered innovations and medical breakthroughs.

DISCUSSION

This work presents a single-step preparable, stiffness-tunable Ga-Cu composite electronic ink capable of high-resolution DIW printing of mechanically transformative electronic circuits for a wide range of designs and applications. We achieved this by incorporating Cu fillers into Ga as rheological modifiers, enabling the Ga-based device layer to function both as a mechanically transformative framework and as an electronic layer. This breakthrough overcame the limitations associated with using pure Ga, which has high surface tension and low viscosity, enabling the creation of intricate circuits with microscale electrical traces (~50 μm) that can rapidly transition between soft and rigid states at body temperature. With these attractive features, we successfully demonstrated an ultrathin epidermal PPG sensor and a wireless optoelectronic device capable of converting between flexible and rigid configurations for biomedical applications. These devices showcase seamless conformal contact on irregular skin surfaces and high deformability, allowing them to adapt to tissue deformation while reliably sensing physiological signals and providing wireless optical stimulation, respectively.

To expedite the soft-to-rigid conversion of our TES beyond the cold-water immersion demonstrated in Fig. 4G, various alternative strategies can be implemented. These may include (i) introducing nucleation agents to the ink, (ii) integrating microfluidic thermal actuators, (iii) attaching flexible thermoelectric device, and (iv) using cryogen spray cooling. Nucleation agents promote supercooling of Ga, by accelerating the phase transition (*9*). In addition, tailoring the microfluidic actuator to the size and pattern of TES enables selective cooling without any adverse effects on the surrounding skin (*8*). Flexible thermoelectric device also enables active and rapid control over the device temperature by supplying input currents (*9*). In clinical settings, cryogen spray cooling (*59*), widely adopted in laser dermatologic surgeries, can precisely cool skin tissues below −40°C with minimal epidermal damage. These comprehensive strategies underscore the efficiency and versatility of our device in applications ranging from everyday use to therapeutic contexts.

Given the demonstrated characteristics and applications, we anticipate that our Ga-Cu composite ink, combined with DIW printing, can unlock new possibilities for next-generation transformative wearable, implantable, ingestible electronics, and various other applications. This innovation would overcome the limitations of contemporary electronics, which typically have invariant mechanical property, being either exclusively soft or rigid. One challenge to address is the potential hardening of the Ga-Cu composite into a brittle intermetallic phase, although this phenomenon was not observed during our studies for at least 8 weeks. In this regard, future research and development that focus on ensuring the long-term stability of Ga-Cu composite ink would be necessary to enhance the long-term reliability of fabricated transformative electronics.

MATERIALS AND METHODS

Fabrication of Ga-Cu ink

Ga-Cu composite ink was prepared by sonicating bulk liquid Ga (Ga metal, 99.99%, RUICHI Changsha Rich Nonferrous Metals) with 5.0 wt % of copper powder (Cu powder, spheroidal, 10 to 25 μm, 98%; Sigma-Aldrich). For homogenous dispersion of Cu in Ga, the mixture was tip-sonicated (VC 505, Sonics & Materials; 3-mm microtip) at an amplitude of 30% and a power intensity of 500 W and 20 kHz for 5 min (fig. S2). Subsequently, the composite was stored at 60°C to facilitate interdiffusion between liquid Ga and Cu fillers, before use for printing (*27*).

Printing process of Ga-Cu composite ink

A DIY 3D printer (Anet A8 Desktop Prusa i3 DIY kit) was used as the skeleton for printing. An interface connecting the extrusion head and the nozzle tip was fabricated using the stereolithographic process with ultraviolet-curable photopolymer (B9R-4-Yellow, B9 Creations). The desired pattern was initially modeled using Rhinoceros 7 as a stereolithography file and was then sliced into G-code (Ultimaker Cura) for printing. 3D printer was connected to a syringe pump (NE-Ne-1000) to apply a consistent pneumatic pressure to the syringe containing 5 ml of the prepared ink. The ink was extruded through a syringe connected to the nozzle tip via a Teflon tube (Tefzel; outer diameter, 1600 μm; inner diameter, 254 μm). Various nozzles (23, 25, 27, and 32 gauges; CELLINK) were used. During the printing process, the distance between the nozzle tip and the substrate was maintained at 1 mm. For device fabrication, the printing speed and extrusion pressures were optimized, varying between 1 and 55 mm s^{-1} and between 10 and 24 kPa, respectively, depending on its purpose. To ensure smooth ink flow without clogging, the Ga-Cu ink was preheated to 60°C to guarantee smooth printing from the nozzle by extending its freezing time. In addition, the printer bed temperature was set to 50°C throughout the entire printing process. When lifted off the preprinted pattern, the nozzle moved along the *z* axis with a velocity ranging between 4 and 30 mm s^{-1}, generating vertical pillars of various heights (2 to 30 mm) as shown in Figs. 2D (bottom) and 3B and fig. S9. At a lift-off velocity of above 30 mm s^{-1}, the printed line fractures as soon as the nozzle leaves the substrate, without forming any vertical pillars.

Characterization on the morphology of Ga-Cu composite ink and thickness of its printed lines

To confirm the homogeneous dispersion of Cu fillers in bulk Ga after 5 min of sonication, field-emission scanning electron microscope (SEM) (JSM-IT800, JEOL) images and EDS mapped images of the solidified samples (1 cm by 1 cm by 0.01 cm) were taken as shown in Fig. 2 (A, B, and the inset of C). In addition, cross-sectional SEM image was taken to prove robust adhesion between bulk Ga and Cu fillers. Line thicknesses were determined through SEM images (Fig. 1A, d). Samples were printed at different printing speeds on a Si wafer for observation.

Rheological characterization for ink optimization

The apparent viscosity of liquid metal inks with different Cu weight percentages (0.0, 2.5, 5.0, and 7.5 wt %) was measured using a rheometer (MCR 302, Anton Paar) at a shear rate ranging from 0 to 10^2 s^{-1} under 55°C. Measurements were conducted three times for each sample, using 100 μl of ink for testing. To assess the wettability of the printed ink on diverse substrates (PDMS, VHB, and SEBS), images of ink droplets were taken by a digital microscope KH-8700 (Hirox). In this procedure, Ga-Cu composite droplets (10 μl) were dropped on these substrates. Then, the droplets were exposed to hydrochloric acid (HCl; 37 wt %) to remove the naturally forming oxide layer from the droplet surface (*9*). The ink wettability of different weight

percentages of Cu (0.0, 2.5, 5.0, and 7.5 wt %) was observed through optical images taken with a contact angle analyzer (Phoenix SEO).

Infrared observation of the phase changing behavior of the Ga-Cu composite

To investigate the phase transition of the Ga-Cu composite, a sample (1 cm by 1 cm by 0.01 cm) was printed with Ga-Cu composite of various weight percentages of Cu (0.0, 2.5, 5.0, and 7.5 wt %). For melting process, the sample was initially kept at room temperature (25°C) and then thawed at a hot plate of 45°C. For freezing process, the same 1-cm by 1-cm by 0.01-cm sample was initially kept at 35°C on a hot plate and was cooled on a cool plate (CP-200TT, TE Technology) at 5°C. The phase changing of the composite was recorded using an infrared camera (A566sc, FLIR) and was plotted with FLIR software program.

Mechanical modeling and finite element analysis

Bending stiffness of the Ga-Cu composite–based samples was simulated through commercial finite element analysis software (COMSOL Multiphysics, COMSOL Inc.). To investigate the bending stiffness of printed Ga-Cu samples at soft and rigid modes, 3D models were built for Ga composite–based samples dispersed with 5.0 wt % of Cu fillers. Considering the size (10 to 25 μm) and shape (spheroidal) of Cu fillers used in the experiment, 680 grains of Cu were embedded to the 50-μm-thick Ga samples, 1360 grains for 100-μm samples, and 2040 grains for 150-μm samples. The samples have various thicknesses (50, 100, and 150 μm), encapsulated with 50-μm-thick PDMS (Young's modulus, 600 kPa) at both the top and bottom. Deflection of each sample was obtained by imposing a downward pressure of 1 mN and 10 μN for rigid mode and soft mode, respectively. The degree of deflection was used to calculate simulated bending stiffness values through the equation $EI = FL^3 / 3\Delta z$, where EI = bending stiffness, F = applied force, L = length, and Δz = deflection (*9*).

Electrical and electromechanical characterization

The resistance of Ga-Cu composite was measured using a four-point probe (2420 Source Meter, Keithley) with a digital multimeter, and the resistivity was calculated using the formula $\rho = R \times w \times t / l$, where ρ represents the resistivity, R is resistance, w is the width of the sample, t is the thickness, and l is the length. Thickness, width, and length of the sample were 0.01, 0.1, and 0.1 cm, respectively. The conductivity is the inverse of resistivity, and the obtained conductivity values for both soft and rigid modes were plotted in fig. S12. For electromechanical characterization (Fig. 3, I and J), a dogbone-shaped pattern was printed with thickness of 100 μm on a VHB substrate. The stretching test and cycling test were conducted for three samples at rigid and soft modes, and their real-time resistance according to strain was measured with an inductance (L), capacitance (C), resistance (R) (LCR) meter (4284A, HP).

Circuit design and signal processing of transformative epidermal PPG sensor

The PPG sensor circuit is depicted in fig. S15. The intensity of red light emitted by the LED (755-CSL1901VW1, Kingbright; 632 nm) was controlled through 100-ohm resistor (R1; ERA-2ARB101X), and the emitted light was captured by the photodiode (ALS-PT19-315C/L177/TR8, Everlight Electronics; 630 nm). Then, the current from the photodiode was converted to a voltage through the 10-kilohm resistor (R2; RC1005F103CS, Samsung Electro-Mechanics). Subsequently, high-frequency noise was eliminated by a capacitor network, which serves a low-pass filter with a cutoff frequency of 20 Hz (*60*). The resulting AC PPG signals were amplified by a factor of 1700 through an inverting amplifier comprising 2.7-kilohm resistor (R3; ERJ-2GEJ272X, Panasonic), 4.8-megohm resistor (R4; RMCF0402FT4M75, Stackpole Electronics), and an operational amplifier (TSV6192IST, STMicroelectronics). Meanwhile, the DC offset was maintained at half voltage common collector through two 100-kilohm resistors (R5 and R6; ERA-2AED104X, Panasonic). The processed PPG signal was captured using an oscilloscope (MSOX2004A, Keysight). The generated signals were further processed using the noise filtering function in MATLAB.

Fabrication of transformative epidermal PPG sensor

The fabrication started with preparation of the device substrate. For the substrate, SEBS solution was prepared by dissolving 3 g of polymer binders in cyclohexane (ACS reagent, >99%; Sigma-Aldrich) at a concentration of 50 mg ml^{-1}. The mixtures were vigorously stirred at 60°C for 24 hours. Dextran (M_r ~ 100,000; Sigma-Aldrich) was diluted into deionized water at a concentration of 50 mg ml^{-1} and spun onto glass slides at 1500 rpm for 45 s. The samples were dried on a hotplate at 150°C for 5 min. The dextran-coated glass slide was spin-coated with SEBS mixture at 750 rpm (10 μm). Then, it was put in a fume hood overnight at ambient temperature to fully evaporate the cyclohexane solvent. The step-by-step fabrication process of dextran-SEBS substrate was illustrated in fig. S16.

For fabrication of the circuit layout, the top and bottom layer interconnects (100 μm) were each printed on SEBS-dextran-glass substrate. To dissolve the dextran sacrificial layer between SEBS layer and the glass slide, the substrate was submerged in room-temperature water. After 10 s, dextran was fully dissolved, and the SEBS layer was gently peeled off from the glass substrate without damage. Upon printing both the top and bottom layers, two VIA holes were manually punched in the top layer and were precisely aligned with corresponding holes in the bottom layer. These holes were then filled with Ga-Cu composite ink to establish electrical connections between the two layers. Electronic chips were mounted onto the interconnects using silver epoxy paste (ELCOAT A-200). Before use, the device was encapsulated with a 10-μm-thick layer of SEBS.

Circuit design of transformative wireless optoelectronic device

The wireless optoelectronic device features a two-layer design, with the coil antenna, the SMD components, and the majority of traces located on the top layer, and only a few traces on the bottom layer. All SMD components (e.g., capacitors, resistors, Schottky diodes, and an LED) within the circuit, except a linear voltage regulator (NCP4624DMU30TCG, ON Semiconductor; 1.0 mm by 1.0 mm by 0.6 mm) and a BLE SoC (RFD77101, RF Digital Corporation; 7 mm by 10 mm by 2.2 mm), have been standardized to a size of 1005 metric (~1.0 mm in width by 0.5 mm in length). The wireless energy harvesting circuit consists of a circular coil antenna (inner diameter, 27 mm; outer diameter, 36 mm) and a DC voltage quadrupler circuit, and the circuit was aimed to tune the antenna to the resonance frequency of 13.56 MHz. The coil antenna was designed to have six turns of 400-μm-wide trace on a single layer. The DC voltage quadrupler circuit consists of (i) a 30-pF capacitor (GRM1555C1H101GA01D,

Murata Electronics) to match the resonant frequency, connected parallel to the coil antenna; (ii) four pairs of Schottky diode (CDBQR0130L, Comchip Technology) and a 4.7-μF charge pump capacitor (GRM155R60J475ME47D, Murata Electronics) to amplify the amplitude of the RF signal by a factor of 4; and (iii) an additional Schottky diode to mitigate reverse current flow, connected in series to the LiPo battery (12 mA·hour ; GMB-300910, PowerStream Technology). Wirelessly charged LiPo battery supplies stable DC current to the BLE SoC through a linear voltage regulator and two 0.1-μF decoupling capacitors (GRM155R61A104JA01D, Murata Electronics). A red LED (VAOL-S4RP4, voltage common collector; 624 nm) for optical stimulation is connected to the output pin of the BLE SoC to be wirelessly operated through BLE communication.

Fabrication of transformative wireless optoelectronic device

Schematic illustration of the overall fabrication process of optoelectronic device is outlined in fig. S17. Initially, the top and bottom layers of interconnects were printed at widths of 100, 200, 300, and 400 μm depending on their purposes, and both layers were printed on a 200-μm-thick SEBS substrate, respectively. After printing, 15 VIAs were manually punched on the top layer, and the top layer was precisely aligned with the corresponding VIA holes on the bottom layer for electrical connections. These VIA holes were filled with Ga-Cu composite ink for an electrical connection between the top and bottom circuits. Then, 17 chips (seven capacitors, two resistors, five Schottky diodes, a LED, a voltage regulator, and a BLE SoC) were mounted on the Ga-Cu composite electrodes on printed on the SEBS layer, using conductive silver epoxy.

Experiments on human individuals

All experiments on human skins were performed under approval from Institutional Review Board at Korea Advanced Institute of Science and Technology (protocol number: KH2018-35) and received informed consent from the volunteer individuals.

Statistical and data analysis

Figures 2E and 3G contained averaged plots for three samples ($N = 3$). All data in Figs. 2H and 3 (D and E) and fig. S7B showed means with SDs ($N = 3$). Figure 2F and fig. S12 showed means and SDs ($N = 4$). All data were analyzed with Origin (OriginPro).

Supplementary Materials

This PDF file includes:

Figs. S1 to S19
Table S1
Legends for movies S1 and S2

Other Supplementary Material for this manuscript includes the following:

Movies S1 and S2

REFERENCES AND NOTES

1. S.-H. Byun, J. Y. Sim, Z. Zhou, J. Lee, R. Qazi, M. C. Walicki, K. E. Parker, M. P. Haney, S. H. Choi, A. Shon, G. B. Gereau, J. Bilbily, S. Li, Y. Liu, W.-H. Yeo, J. G. McCall, J. Xiao, J.-W. Jeong, Mechanically transformative electronics, sensors, and implantable devices. *Sci. Adv.* **5**, eaay0418 (2019).
2. S.-H. Byun, J. Y. Sim, K.-C. Agno, J.-W. Jeong, Materials and manufacturing strategies for mechanically transformative electronics. *Mater. Today Adv.* **7**, 100089 (2020).
3. D.-H. Kim, N. Lu, R. Ma, Y.-S. Kim, R.-H. Kim, S. Wang, J. Wu, S. M. Won, H. Tao, A. Islam, K. J. Yu, T. Kim, R. Chowdhury, M. Ying, L. Xu, M. Li, H.-J. Chung, H. Keum, M. McCormick, P. Liu, Y.-W. Zhang, F. G. Omenetto, Y. Huang, T. Coleman, J. A. Rogers, Epidermal electronics. *Science* **333**, 838–843 (2011).
4. J.-W. Jeong, J. G. McCall, G. Shin, Y. Zhang, R. Al-Hasani, M. Kim, S. Li, J. Y. Sim, K.-I. Jang, Y. Shi, D. Y. Hong, Y. Liu, G. P. Schmitz, L. Xia, Z. He, P. Gamble, W. Z. Ray, Y. Huang, M. R. Bruchas, J. A. Rogers, Wireless optofluidic systems for programmable in vivo pharmacology and optogenetics. *Cell* **162**, 662–674 (2015).
5. Y. Jiang, Z. Zhang, Y.-X. Wang, D. Li, C.-T. Coen, E. Hwaun, G. Chen, H.-C. Wu, D. Zhong, S. Niu, W. Wang, A. Saberi, J.-C. Lai, Y. Wu, Y. Wang, A. A. Trotsyuk, K. Y. Loh, C.-C. Shih, W. Xu, K. Liang, K. Zhang, Y. Bai, G. Gurusankar, W. Hu, W. Jia, Z. Cheng, R. H. Dauskardt, G. C. Gurtner, J. B.-H. Tok, K. Deisseroth, I. Soltesz, Z. Bao, Topological supramolecular network enabled high-conductivity, stretchable organic bioelectronics. *Science* **375**, 1411–1417 (2022).
6. G.-H. Lee, H. Kim, J. Lee, J.-Y. Bae, C. Yang, H. Kim, H. Kang, S. Q. Choi, S. Park, S.-K. Kang, J. Kang, Z. Bao, J.-W. Jeong, S. Park, Large-area photo-patterning of initially conductive EGaIn particle-assembled film for soft electronics. *Mater. Today* **67**, 84–94 (2023).
7. S. Cho, H. J. Nam, C. Shi, C. Y. Kim, S.-H. Byun, K.-C. Agno, B. C. Lee, J. Xiao, J. Y. Sim, J.-W. Jeong, Wireless, AI-enabled wearable thermal comfort sensor for energy-efficient, human-in-the-loop control of indoor temperature. *Biosens. Bioelectron.* **223**, 115018 (2023).
8. S. Lee, S.-H. Byun, C. Y. Kim, S. Cho, S. Park, J. Y. Sim, J.-W. Jeong, Beyond human touch perception: An adaptive robotic skin based on gallium microgranules for pressure sensory augmentation. *Adv. Mater.* **34**, e2204805 (2022).
9. S.-H. Byun, C. S. Kim, K.-C. Agno, S. Lee, Z. Li, B. J. Cho, J.-W. Jeong, Design strategy for transformative electronic system toward rapid, bidirectional stiffness tuning using graphene and flexible thermoelectric device interfaces. *Adv. Mater.* **33**, e2007239 (2021).
10. K.-C. Agno, K. Yang, S.-H. Byun, S. Oh, S. Lee, H. Kim, K. Kim, S. Cho, W.-I. Jeong, J.-W. Jeong, A temperature-responsive intravenous needle that irreversibly softens on insertion. *Nat. Biomed. Eng.*, https://doi.org/10.1038/s41551-023-01116-z (2023).
11. S. Oh, S. Lee, S.-H. Byun, S. Lee, C. Y. Kim, J. Yea, S. Chung, S. Li, K.-I. Jang, J. Kang, J.-W. Jeong, 3D shape-morphing display enabled by electrothermally responsive, stiffness-tunable liquid metal platform with stretchable electroluminescent device. *Adv. Funct. Mater.* **33**, 2214766 (2023).
12. S.-H. Byun, J. H. Yun, S.-Y. Heo, C. Shi, G. J. Lee, K.-C. Agno, K.-I. Jang, J. Xiao, Y. M. Song, J.-W. Jeong, Self-cooling gallium-based transformative electronics with a radiative cooler for reliable stiffness tuning in outdoor use. *Adv. Sci. (Weinh)* **9**, e2202549 (2022).
13. Y. Bar-Cohen, I. A. Anderson, Electroactive polymer (EAP) actuators—Background review. *Mech. Soft Mater.* **1**, 5 (2019).
14. Q. Wang, C. Pan, Y. Zhang, L. Peng, Z. Chen, C. Majidi, L. Jiang, Magnetoactive liquid-solid phase transitional matter. *Matter* **6**, 855–872 (2023).
15. C. Ni, D. Chen, Y. Yin, X. Wen, X. Chen, C. Yang, G. Chen, Z. Sun, J. Wen, Y. Jiao, C. Wang, N. Wang, X. Kong, S. Deng, Y. Shen, R. Xiao, X. Jin, J. Li, X. Kong, Q. Zhao, T. Xie, Shape memory polymer with programmable recovery onset. *Nature* **622**, 748–753 (2023).
16. Y. Lin, J. Genzer, M. D. Dickey, Attributes, fabrication, and applications of gallium-based liquid metal particles. *Adv. Sci. (Weinh)* **7**, 2000192 (2020).
17. M. D. Dickey, Stretchable and soft electronics using liquid metals. *Adv. Mater.* **29**, 1606425 (2017).
18. S.-Y. Tang, C. Tabor, K. Kalantar-Zadeh, M. D. Dickey, Gallium liquid metal: The devil's elixir. *Annu. Rev. Mater. Res.* **51**, 381–408 (2021).
19. S. P. Lacour, Epidermal electronics: Skin health monitoring. *Nat. Mater.* **14**, 659–660 (2015).
20. R. R. Suresh, M. Lakshmanakumar, A. Jayalatha J. B. B., K. S. Rajan, S. Sethuraman, U. M. Krishnan, J. B. B. Rayappan, Fabrication of screen-printed electrodes: Opportunities and challenges. *J. Mater. Sci.* **56**, 8951–9006 (2021).
21. Y. Wang, J. Chen, Z. Yin, Y. Li, A high-adaptability nozzle-array printing system based on a set covering printing planning model for printed display manufacturing. *Sci. Rep.* **13**, 156 (2023).
22. R. Y. Tay, Y. Song, D. R. Yao, W. Gao, Direct-ink-writing 3D-printed bioelectronics. *Mater. Today (Kidlington)* **71**, 135–151 (2023).
23. G.-H. Lee, Y. R. Lee, H. Kim, D. A. Kwon, H. Kim, C. Yang, S. Q. Choi, S. Park, J.-W. Jeong, S. Park, Rapid meniscus-guided printing of stable semi-solid-state liquid metal microgranular-particle for soft electronics. *Nat. Commun.* **13**, 2643 (2022).
24. Y.-G. Park, H. S. An, J.-Y. Kim, J.-U. Park, High-resolution, reconfigurable printing of liquid metals with three-dimensional structures. *Sci. Adv.* **5**, eaaw2844 (2019).
25. Y.-G. Park, I. Yun, W. G. Chung, W. Park, D. H. Lee, J.-U. Park, High-resolution 3D printing for electronics. *Adv. Sci. (Weinh)* **9**, e2104623 (2022).
26. C. Wang, Y. Gong, B. V. Cunning, S. Lee, Q. Le, S. R. Joshi, O. Buyukcakir, H. Zhang, W. K. Seong, M. Huang, M. Wang, J. Lee, G.-H. Kim, R. S. Ruoff, A general approach to composites containing nonmetallic fillers and liquid gallium. *Sci. Adv.* **7**, eabe3767 (2021).
27. D. P. Parekh, C. M. Fancher, M. G. Mohammed, T. V. Neumann, D. Saini, J. Guerrier, C. Ladd, E. Hubbard, J. L. Jones, M. D. Dickey, Liquid–solid mixtures of Ga metal infused with Cu microparticles and nanoparticles for microscale and nanoscale patterning of solid metals at room temperature. *ACS Appl. Nano Mater.* **3**, 12064–12070 (2020).
28. A. Samal, A. K. Kushwaha, D. Das, M. R. Sahoo, N. A. Lanzillo, S. K. Nayak, Thermal and electrical conductivity of copper-graphene heterosystem: An effect of strain and thickness. *Adv. Eng. Mater.* **25**, 2201192 (2023).

29. Y. Feng, X. Wang, F. Xiao, Low-temperature calcination of convenient micro-sized copper ink with surface activation and synchronous protection by in-situ chemisorbed cupric formate. *J. Mater. Sci. Mater. Electron.* **33**, 19297–19306 (2022).
30. J. Tang, X. Zhao, J. Li, R. Guo, Y. Zhou, J. Liu, Gallium-based liquid metal amalgams: Transitional-state metallic mixtures (TransM2ixes) with enhanced and tunable electrical, thermal, and mechanical properties. *ACS Appl. Mater. Interfaces* **9**, 35977–35987 (2017).
31. X. Wang, X. Liu, P. Bi, Y. Zhang, L. Li, J. Guo, Y. Zhang, X. Niu, Y. Wang, L. Hu, Y. Fan, Electrochemically enabled embedded three-dimensional printing of freestanding gallium wire-like structures. *ACS Appl. Mater. Interfaces* **12**, 53966–53972 (2020).
32. X. Wang, D. V. M. Repaka, A. Suwardi, Q. Zhu, J. Wu, J. Xu, Thermal and electrical properties of liquid metal gallium during phase transition. *Trans. Tianjin Univ.* **29**, 209–215 (2023).
33. Z. Baig, O. Mamat, M. Mustapha, A. Mumtaz, K. S. Munir, M. Sarfraz, Investigation of tip sonication effects on structural quality of graphene nanoplatelets (GNPs) for superior solvent dispersion. *Ultrason. Sonochem.* **45**, 133–149 (2018).
34. H. Wang, W. Xing, S. Chen, C. Song, M. D. Dickey, T. Deng, Liquid metal composites with enhanced thermal conductivity and stability using molecular thermal linker. *Adv. Mater.* **33**, 2103104 (2021).
35. V. Y. Prokhorenko, V. V. Roshchupkin, M. A. Pokrasin, S. V. Prokhorenko, V. V. Kotov, Liquid gallium: Potential uses as a heat-transfer agent. *High Temp.* **38**, 954–968 (2000).
36. B. Barker, J. B. Bell, A. L. Garcia, Fluctuating hydrodynamics and the Rayleigh–Plateau instability. *Proc. Natl. Acad. Sci. U.S.A.* **120**, e2306088120 (2023).
37. S. Handschuh-Wang, F. J. Stadler, X. Zhou, Critical review on the physical properties of gallium-based liquid metals and selected pathways for their alteration. *J. Phys. Chem. C* **125**, 20113–20142 (2021).
38. J.-W. Jeong, W.-H. Yeo, A. Akhtar, J. J. S. Norton, Y.-J. Kwack, S. Li, S.-Y. Jung, Y. Su, W. Lee, J. Xia, H. Cheng, Y. Huang, W.-S. Choi, T. Bretl, J. A. Rogers, Materials and optimized designs for human-machine interfaces via epidermal electronics. *Adv. Mater.* **25**, 6839–6846 (2013).
39. Y. Liu, J. J. S. Norton, R. Qazi, Z. Zou, K. R. Ammann, H. Liu, L. Yan, P. L. Tran, K.-I. Jang, J. W. Lee, D. Zhang, K. A. Kilian, S. H. Jung, T. Bretl, J. Xiao, M. J. Slepian, Y. Huang, J.-W. Jeong, J. A. Rogers, Epidermal mechano-acoustic sensing electronics for cardiovascular diagnostics and human-machine interfaces. *Sci. Adv.* **2**, e1601185 (2016).
40. J. J. S. Norton, D. S. Lee, J. W. Lee, W. Lee, O. Kwon, P. Won, S.-Y. Jung, H. Cheng, J.-W. Jeong, A. Akce, S. Umunna, I. Na, Y. H. Kwon, X.-Q. Wang, Z. Liu, U. Paik, Y. Huang, T. Bretl, W.-H. Yeo, J. A. Rogers, Soft, curved electrode systems capable of integration on the auricle as a persistent brain–computer interface. *Proc. Natl. Acad. Sci. U.S.A.* **112**, 3920–3925 (2015).
41. L. Tian, B. Zimmerman, A. Akhtar, K. J. Yu, M. Moore, J. Wu, R. J. Larsen, J. W. Lee, J. Li, Y. Liu, B. Metzger, S. Qu, X. Guo, K. E. Mathewson, J. A. Fan, J. Cornman, M. Fatina, Z. Xie, Y. Ma, J. Zhang, Y. Zhang, F. Dolcos, M. Fabiani, G. Gratton, T. Bretl, L. J. Hargrove, P. V. Braun, Y. Huang, J. A. Rogers, Large-area MRI-compatible epidermal electronic interfaces for prosthetic control and cognitive monitoring. *Nat. Biomed. Eng.* **3**, 194–205 (2019).
42. J. Jeong, M. K. Kim, H. Cheng, W. Yeo, X. Huang, Y. Liu, Y. Zhang, Y. Huang, J. A. Rogers, Capacitive epidermal electronics for electrically safe, long-term electrophysiological measurements. *Adv. Healthc. Mater.* **3**, 642–648 (2014).
43. D.-H. Kim, J. Viventi, J. J. Amsden, J. Xiao, L. Vigeland, Y.-S. Kim, J. A. Blanco, B. Panilaitis, E. S. Frechette, D. Contreras, D. L. Kaplan, F. G. Omenetto, Y. Huang, K.-C. Hwang, M. R. Zakin, B. Litt, J. A. Rogers, Dissolvable films of silk fibroin for ultrathin conformal bio-integrated electronics. *Nat. Mater.* **9**, 511–517 (2010).
44. J. M. Stankiewicz, Analysis of the influence of the skin effect on the efficiency and power of the receiver in the periodic WPT system. *Energies* **16**, 2009 (2023).
45. A. Mueed, Y. Zhao, W. Yan, S. Khan, Q. Q. Liu, C. Huang, Skin effect and proximity effect analysis of stranded conductor based on mixed order MoM with adaptive cross approximation algorithm. *Eng. Anal. Bound. Elem.* **120**, 52–58 (2020).
46. R. B. Keller, Skin effect, in *Design for Electromagnetic Compatibility--In a Nutshell: Theory and Practice*, R. B. Keller, Ed. (Springer International Publishing, 2023), pp. 135–143.
47. R. Justice, Skin effect antennas, U.S. Patent US4571592A (1986); https://patents.google.com/patent/US4571592A/en.
48. W. Wang, X. Wu, K. W. Kevin Tang, I. Pyatnitskiy, R. Taniguchi, P. Lin, R. Zhou, S. L. C. Capocyan, G. Hong, H. Wang, Ultrasound-triggered in situ photon emission for noninvasive optogenetics. *J. Am. Chem. Soc.* **145**, 1097–1107 (2023).
49. "Technical data sheet: 3M™ VHB™ tape - Specialty tape 4905". https://technicaldatasheets.3m.com/en_US?pif=000343.
50. C. Y. Kim, M. J. Ku, R. Qazi, H. J. Nam, J. W. Park, K. S. Nam, S. Oh, I. Kang, J.-H. Jang, W. Y. Kim, J.-H. Kim, J.-W. Jeong, Soft subdermal implant capable of wireless battery charging and programmable controls for applications in optogenetics. *Nat. Commun.* **12**, 535 (2021).
51. R. Qazi, A. M. Gomez, D. C. Castro, Z. Zou, J. Y. Sim, Y. Xiong, J. Abdo, C. Y. Kim, A. Anderson, F. Lohner, S.-H. Byun, B. Chul Lee, K.-I. Jang, J. Xiao, M. R. Bruchas, J.-W. Jeong, Wireless optofluidic brain probes for chronic neuropharmacology and photostimulation. *Nat. Biomed. Eng.* **3**, 655–669 (2019).
52. J. Lee, K. E. Parker, C. Kawakami, J. R. Kim, R. Qazi, J. Yea, S. Zhang, C. Y. Kim, J. Bilbily, J. Xiao, K. Jang, J. G. McCall, J.-W. Jeong, Rapidly customizable, scalable 3D-printed wireless optogenetic probes for versatile applications in neuroscience. *Adv. Funct. Mater.* **30**, 2004285 (2020).
53. R. Qazi, K. E. Parker, C. Y. Kim, R. Rill, M. R. Norris, J. Chung, J. Bilbily, J. R. Kim, M. C. Walicki, G. B. Gereau, H. Lim, Y. Xiong, J. R. Lee, M. A. Tapia, A. V. Kravitz, M. J. Will, S. Ha, J. G. McCall, J.-W. Jeong, Scalable and modular wireless-network infrastructure for large-scale behavioural neuroscience. *Nat. Biomed. Eng.* **6**, 771–786 (2022).
54. K. E. Parker, J. Lee, J. R. Kim, C. Kawakami, C. Y. Kim, R. Qazi, K.-I. Jang, J.-W. Jeong, J. G. McCall, Customizable, wireless and implantable neural probe design and fabrication via 3D printing. *Nat. Protoc.* **18**, 3–21 (2023).
55. R. Qazi, C. Y. Kim, S.-H. Byun, J.-W. Jeong, Microscale inorganic LED based wireless neural systems for chronic in vivo optogenetics. *Front. Neurosci.* **12**, 764 (2018).
56. L. Zhang, Y. Li, L. Yuan, Q. Zhang, Y. Yan, F. Dong, J. Tang, Y. Wang, Advanced and readily-available wireless-powered blue-light-implant for non-invasive peri-implant disinfection. *Adv. Sci. (Weinh)* **10**, e2203472 (2023).
57. W. S. Kim, M. I. Khot, H.-M. Woo, S. Hong, D.-H. Baek, T. Maisey, B. Daniels, P. L. Coletta, B.-J. Yoon, D. G. Jayne, S. I. Park, AI-enabled, implantable, multichannel wireless telemetry for photodynamic therapy. *Nat. Commun.* **13**, 2178 (2022).
58. S. Huang, C. Yang, Z. Liu, X. Huang, H.-J. Chen, Wireless implantable phototherapy device for oral inflammation repair, in *2021 IEEE 16th International Conference on Nano/Micro Engineered and Molecular Systems (NEMS)* (IEEE, 2021), pp. 503–506.
59. B. Chen, J. Tian, R. Wang, Z. Zhou, Theoretical study of cryogen spray cooling with R134a, R404A and R1234yf: Comparison and clinical potential application. *Appl. Therm. Eng.* **148**, 1058–1067 (2019).
60. W. Lee, H. Kim, I. Kang, H. Park, J. Jung, H. Lee, H. Park, J. S. Park, J. M. Yuk, S. Ryu, J.-W. Jeong, J. Kang, Universal assembly of liquid metal particles in polymers enables elastic printed circuit board. *Science* **378**, 637–641 (2022).
61. H.-T. Fan, L.-Q. Shi, H. Shen, X. Chen, K.-P. Xie, Equilibrium, isotherm, kinetic and thermodynamic studies for removal of tetracycline antibiotics by adsorption onto hazelnut shell derived activated carbons from aqueous media. *RSC Adv.* **6**, 109983–109991 (2016).

Acknowledgments

Funding: This work was supported by National Research Foundation of Korea (NRF-2022M3E5E9017759 and NRF-2022R1A4A5033852, J.-W.J.; NRF-2022R1A2C2006076, S.P.) and Institute of Information and Communications Technology Planning and Evaluation (IITP-2022-0-00025). **Author contributions:** Concept, design, and study direction: D.A.K., S.L., and J.-W.J. Device fabrication: D.A.K. Experimental validation: D.A.K., S.L., I.K., and J.-W.J. Data analysis: D.A.K., S.L., C.Y.K., I.K., S.P., and J.-W.J. Theoretical modeling: D.A.K. and S.L. Manuscript writing: D.A.K., S.L., C.Y.K., S.P., and J.-W.J. Supervision: S.P. and J.-W.J. Projection administration: J.-W.J. **Competing interests:** The authors declare that they have no competing interest. **Data and materials availability:** All data needed to evaluate the conclusions in the paper are present in the paper and/or the Supplementary Materials.

Submitted 23 November 2023
Accepted 29 January 2024
Published 28 February 2024
10.1126/sciadv.adn1186